Title
Imaging in vivo acetylcholine release in the peripheral nervous system with a fluorescent nanosensor

Journal
Proceedings of the National Academy of Sciences of the United States of America, 118(14)

ISSN
0027-8424

Authors
Xia, Junfei
Yang, Hongrong
Mu, Michelle
et al.

Publication Date
2021-04-06

DOI
10.1073/pnas.2023807118

Peer reviewed

Imaging in vivo acetylcholine release in the peripheral nervous system with a fluorescent nanosensor

Junfei Xia[a,1], Hongrong Yang[a,1], Michelle Mu[a], Nicholas Micovic[a], Kira E. Poskanzer[b,c], James R. Monaghan[d], and Heather A. Clark[a,e,2]

[a]Department of Bioengineering, College of Engineering, Northeastern University, Boston, MA 02115; [b]Department of Biochemistry and Biophysics, University of California, San Francisco, CA 94143; [c]Kavli Insititute for Fundamental Neuroscience, San Francisco, CA 94143; [d]Department of Biology, College of Science, Northeastern University, Boston, MA 02115; and [e]Department of Chemistry and Chemical Biology, College of Science, Northeastern University, Boston, MA 02115

Edited by Chad A. Mirkin, Northwestern University, Evanston, IL, and approved February 16, 2021 (received for review November 19, 2020)

The ability to monitor the release of neurotransmitters during synaptic transmission would significantly impact the diagnosis and treatment of neurological diseases. Here, we present a DNA-based enzymatic nanosensor for quantitative detection of acetylcholine (ACh) in the peripheral nervous system of living mice. ACh nanosensors consist of DNA as a scaffold, acetylcholinesterase as a recognition component, pH-sensitive fluorophores as signal generators, and α-bungarotoxin as a targeting moiety. We demonstrate the utility of the nanosensors in the submandibular ganglia of living mice to sensitively detect ACh ranging from 0.228 to 358 μM. In addition, the sensor response upon electrical stimulation of the efferent nerve is dose dependent, reversible, and we observe a reduction of ∼76% in sensor signal upon pharmacological inhibition of ACh release. Equipped with an advanced imaging processing tool, we further spatially resolve ACh signal propagation on the tissue level. Our platform enables sensitive measurement and mapping of ACh transmission in the peripheral nervous system.

nanosensor | acetylcholine | acetylcholinesterase | DNA | submandibular ganglion

The cholinergic system has an important role in nearly every bodily function ranging from muscle contraction, heart rate, gland secretion, inflammation, to cognition and memory. Defects in cholinergic transmission lead to a number of pathologies ranging from Alzheimer's disease and Parkinson's disease in the central nervous system (CNS) (1, 2) to Myasthenia Gravis in the peripheral nervous system (PNS) (3). To understand the many functions of the cholinergic system and the etiology of cholinergic diseases, a longstanding goal has been to develop technologies that allow the sensing and mapping of cholinergic neural communication in vivo (4–7). An obstacle in advancing our understanding of the cholinergic system is the lack of proper techniques for measuring and mapping the spatial and temporal patterns of acetylcholine (ACh) release in organs in real time with satisfactory sensitivity.

It is particularly challenging for standard tools such as microelectrodes and microdialysis to simultaneously obtain spatial and temporal information of ACh release. Accurate local measurement requires precise localization of the probes for spatial resolution and fast response of the probes for temporal information. Yet the size of microelectrodes and microdialysis probes make placement in the CNS and PNS difficult, particularly if multiple probes are to be used simultaneously to gain spatial information. Although microelectrodes have unparalleled temporal response, microdialysis can take minutes. Conversely, microdialysis can specifically identify ACh after extraction, but microelectrodes are more suitable for in vivo detection of catecholamines than inoxidizable ACh (8). The last decade has witnessed considerable progress in improving microdialysis and microeletrodes for neurotransmitter studies. For example, Zhang et al. and Yang et al. shortened the sampling time of microdialysis [typically 5 to 15 min (9)] to only 1 to 2 min for serotonin analysis via instrumentational upgrades (10–12), which enabled the study of serotonin network associated with stress, anxiety, and circadian rhythms (11, 13). Song and coworkers achieved high temporal resolution monitoring of ACh with ∼5 s intervals in the rat brain by a combination of microdialysis sampling, segmented flow, and direct infusion mass spectrometry (14). Additionally, advances have been made to improve the spatial resolution of microelectrodes/fast-scan cyclic voltammetry by combining multiple electrodes into a microarray (15) and minimizing the size of the electrode tip into nanoscale (50 to 400 nm) (16), even under 20 nm to allow access to single synapses in cultured neurons (17). New imaging technologies, such as genetically encoded fluorescent sensors (CNiFERs) and G protein–coupled receptors–based sensors with enhanced quantum yield and sensitivity have advanced in vivo imaging of dopamine, norepinephrine, and ACh in CNS (6, 7, 18–23). To meet this goal, we previously reported a nanosensor to detect ACh with a fluorescent reporter, but it lacks the sensitivity to make quantitative measurements in vivo (24). Despite these compelling breakthroughs, reports on measuring ACh dynamics in real time remain scarce, especially for PNS, illuminating the difficulty of combining the individual strengths of spatial resolution, temporal resolution, and sensitivity into one measurement tool.

Significance

Mapping and measuring neurotransmitter release in vivo provides critical neurological insight into animal behavior and pathology. Acetylcholine, a pleiotropic neurotransmitter, impacts cardiovascular, cognitive, and other physiological functions. To circumvent genetic manipulation and provide high sensitivity as well as temporal and spatial resolution, we developed a DNA-based enzymatic nanosensor for real-time monitoring of acetylcholine release in the PNS of living mice. The nanosensor rapidly responds to endogenous acetylcholine release in a dose-dependent and reversible manner, providing spatial mapping of signal transmission within a single ganglion when combined with advanced image analysis. The nanosensor expands the analytical toolbox for detecting PNS neurotransmission but will also be applicable for the CNS in multiple species, enabling elucidation of fundamental neurological and neuropathological pathways.

Author contributions: J.X., H.Y., J.R.M., and H.A.C. designed research; J.X., H.Y., and M.M. performed research; K.E.P. contributed new reagents/analytic tools; J.X., H.Y., N.M., J.R.M., and H.A.C. analyzed data; and J.X., H.Y., J.R.M., and H.A.C. wrote the paper.

The authors declare no competing interest.

This article is a PNAS Direct Submission.

[1]J.X. and H.Y. contributed equally to this work.

[2]To whom correspondence may be addressed. Email: h.clark@northeastern.edu.

This article contains supporting information online at https://www.pnas.org/lookup/suppl/doi:10.1073/pnas.2023807118/-/DCSupplemental.

Published April 1, 2021.

Here, we report a fluorescent ACh-selective nanosensor to image ACh release and its use in the submandibular ganglion (SMG) of living mice, as a model tissue, to report real-time, quantitative endogenous ACh release triggered by electrical stimulation of the nerve (Fig. 1 *A* and *B*). Our design uses double-stranded DNA as the scaffold, acetylcholinesterase (AChE) as the recognition component, and a pH-sensitive fluorophore (pHAb) as the signal reporter (Fig. 1*C*). Compared to synthetic polymers, using DNA as the sensor scaffold is advantageous because of its ability to form complex structures with a resulting homogeneous size distribution, high yield for ligand attachment to the structure, and exquisite control over positioning of the ligands (25–27). These properties are important because the sensor mechanism requires that we position the pH-senstive fluorophores in close proximity to AChE to report local pH changes in response to ACh hydrolysis. We also include a second ligand, α-bungarotoxin (BTX), to target the nanosensors to nicotinic ACh receptors (28). The BTX is additionally labeled with an Alexa 647 fluorophore (BTX-AF647) spectrally distinct from pHAb and acts as an internal standard, enabling quantitative measurements despite potential variations in sensor number or diffusion in the organ. Although there was little information available on the anticipated ACh concentration range in the SMG, we tuned the performance based on literature for other tissues. We estimated based on reports in the neuromuscular junction and CNS that low- to mid- micromolar to millimolar levels were appropriate (29, 30). We also anticipated that the sensor should have a temporal response of milliseconds or less. As an optical sensor, the signal attenuation due to tissue absorption should be minimized by selecting fluorophores with red or near-infrared wavelength to be compatible with tissue imaging and preferably extensible to techniques such as two-photon microscopy (31). With these properties, the sensor would then be well suited to imaging dynamic ACh release in the SMG as well as future applications in other tissues. Additionally, coupled with the Astrocyte Quantitative Analysis (AQuA) program (32), an advanced imaging processing tool, we further present the propagation of ACh transmission across the whole SMG based on the fluorescence output of the ACh nanosensors.

Results

Fabrication and In Vitro Characterization of ACh Nanosensors. The ACh nanosensors consisted of four functional motifs: DNA scaffold, AChE, pHAb fluorophores, and BTX-AF647. The dendritic, double-stranded DNA scaffold was self-assembled from five DNA oligonucleotides (*SI Appendix*, Table S1). The pHAb fluorophore [3′,6′-bis(4-(4-sulfobutyl)piperazin-1-yl) rhodamine (5′,6′) succinimidyl ester (33)] was selected as the reporter because of its red emission wavelength and "turn on" response when protonated. The pHAb fluorophores were linked to single-stranded DNA (ssDNA) (strands L2, L3, and L4) via *N*-hydroxysuccinimide ester reaction while the other two strands (L1 and L5) were functionalized with tetrazine groups for later attachment to BTX (*SI Appendix*, Fig. S1). After the five ssDNA oligonucleotides were annealed to form a DNA scaffold, AChE was covalently attached to the DNA scaffold via a maleimide–succinimidyl ester cross-linker (maleimide linker) conjugating the primary amine of lysine residues on AChE to the thiol-terminated DNA strands (Fig. 2*B*). The extremely high catalytic activity of AChE ensures rapid hydrolysis of ACh in a highly specific manner (34). BTX was chosen as a targeting ligand because it has been widely recognized to bind to nicotinic ACh receptors in a highly selective and efficient manner (35). A transcyclooctene (TCO)–succinimidyl ester cross-linker (TCO linker) was conjugated to the surface lysine of BTX-AF647 and further reacted with a tetrazine-terminated DNA via a Click reaction (Fig. 2*C*).

Fully assembled ACh nanosensors were purified by size-exclusion high-performance liquid chromatography (HPLC). A typical chromatogram of the reaction mixture (Fig. 2*D*) showed well-resolved and reproducible peaks across different batches. ACh nanosensors eluted first (Main peak) due to its high molecular weight, with a retention volume of ∼7.5 mL and was identified by three characteristic absorbance spectra (i.e., λabs = 260 nm for DNA, 280 nm for protein, and 652 nm for AF647) and an emission spectrum of the pHAb fluorophore (i.e., λex = 532 and λem = 560 nm). The following peak with the retention volume of 9.1 to 9.2 mL included unreacted DNA scaffolds, AChE, and BTX-conjugated DNA scaffolds (Second peak). It

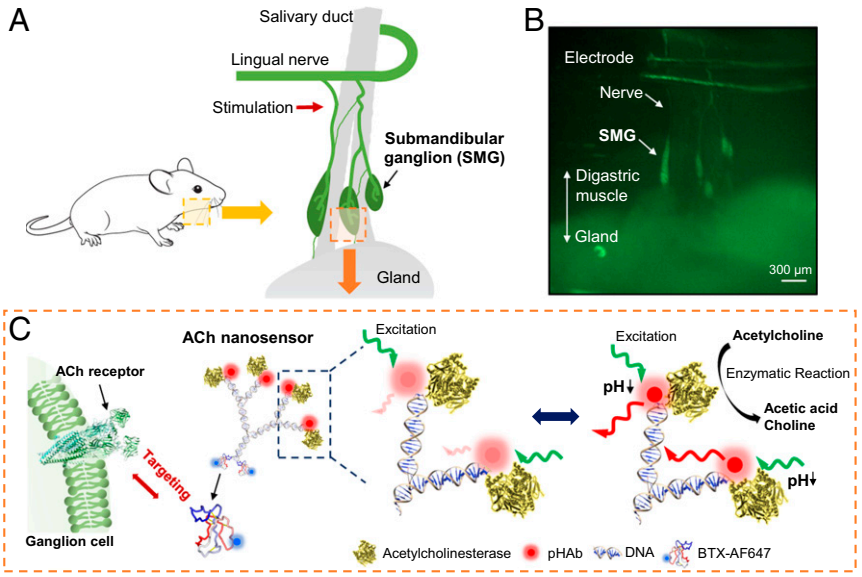

Fig. 1. Design of nanosensor for in vivo imaging of ACh release. (*A*) A schematic showing the SMGs located on the salivary duct that connects the digastric muscle to the salivary gland. (*B*) An image of the SMG in a ChAT(BAC)-eGFP transgenic mouse showing green fluorescent protein expression in presynaptic axons and postsynaptic neurons. The location of the stimulation electrode is indicated. (*C*) A schematic showing ACh nanosensor structure and mechanism for ACh detection. Nanosensors are targeted to ACh receptors via the conjugated BTX. AChE linked to the DNA scaffold hydrolyzes ACh and lowers local pH through the production of acetic acid. Four pH-sensitive pHAb fluorophores are in close proximity to AChE and increase fluorescent emission in response to ACh hydrolysis. AF647 on the BTX acts as an internal standard to enable quantitative measurements.

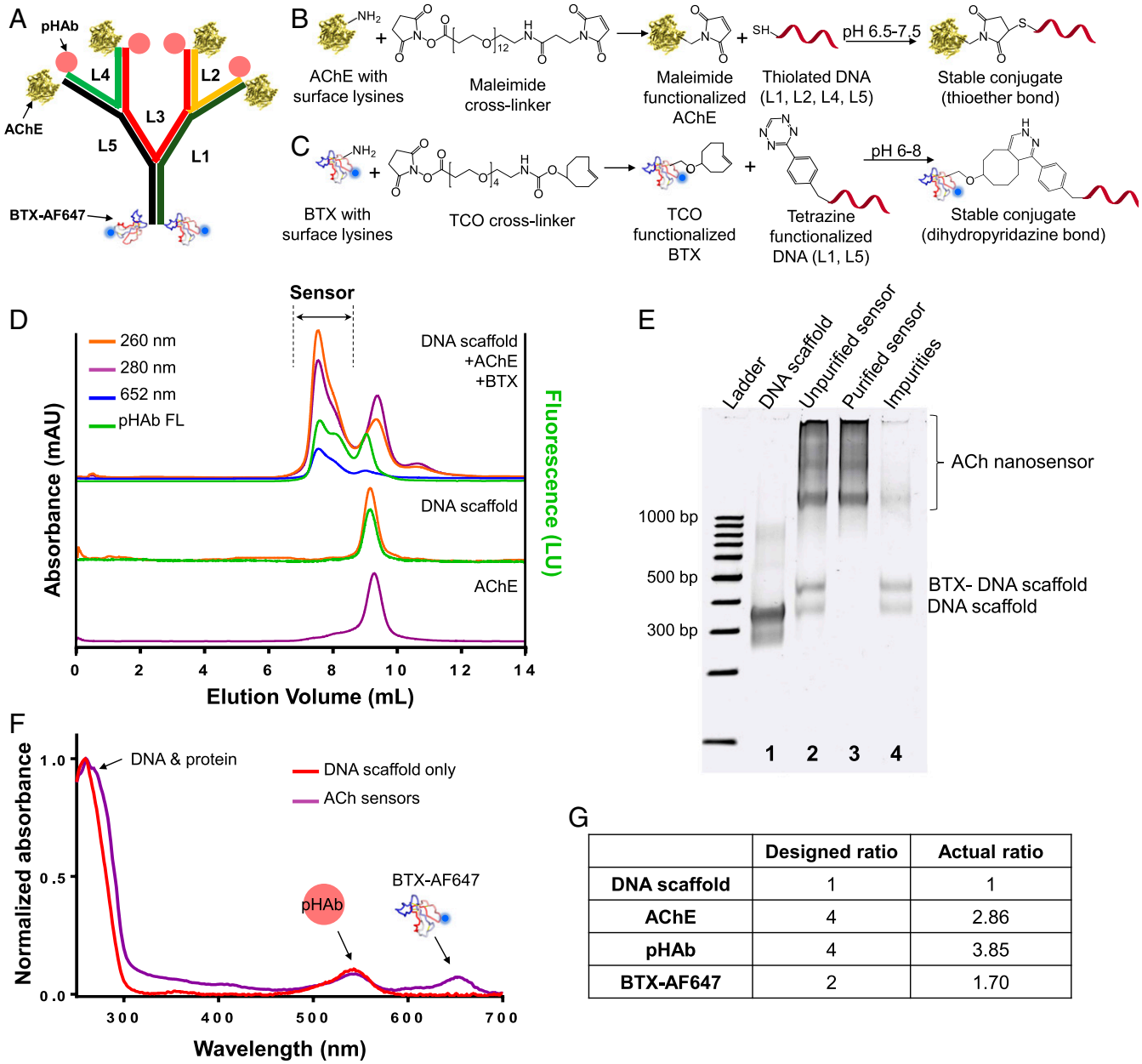

G

	Designed ratio	Actual ratio
DNA scaffold	1	1
AChE	4	2.86
pHAb	4	3.85
BTX-AF647	2	1.70

Fig. 2. Successful bottom-up assembly and purification of ACh nanosensors. (*A*) The ACh nanosensors consisted of four components: DNA scaffold (five strands, designated L1 to L5), AChE as a recognition motif, pHAb fluorophore as a pH reporter, and BTX as a targeting molecule. (*B*) Conjugation of AChE to DNA scaffold via maleimide–thiol chemistry. (*C*) Conjugation of BTX to DNA scaffold via TCO–tetrazine click chemistry. (*D*) Fully assembled ACh nanosensors were purified by size-exclusion HPLC. Eluted samples from top to bottom are the reaction mixture that contained DNA scaffold, BTX and AChE; DNA scaffold only; AChE only. Three ultraviolet–visible (UV-Vis) signals and one fluorescent signal were monitored during HPLC elution. Conditions: 150 mM sodium phosphate and 500 mM NaCl (pH = 7.2 to 7.4). (*E*) Native PAGE characterization of the fractions from HPLC in *D* stained with ethidium bromide. Lane 1: DNA scaffold only; Lane 2: unpurified reaction mixture; Lane 3: purified ACh nanosensors (main peak); and Lane 4: impurities that contained unreacted AChE, DNA scaffold, and BTX-conjugated DNA scaffold (second peak). Note that unreacted AChE were not stained in the gel. (*F*) UV-Vis spectra of DNA scaffold and ACh nanosensors indicated successful conjugation of two proteins and pHAb fluorophores. (*G*) The actual conjugation ratios of AChE and BTX on DNA scaffold compared to designed ratios.

was estimated that ACh nanosensors represent ~77% of the reaction mixture based on the integration of areas under all detectable peaks from the pHAb channel chromatogram, indicating a high yield in the DNA–protein conjugation. We found that the attachment of BTX to the DNA scaffold alone does not significantly impact the retention time in the Superdex 200 column, evidenced by similar retention times of BTX-conjugated DNA scaffold in HPLC elution (*SI Appendix*, Fig. S2). Note that BTX is a small polypeptide (~8,000 Da) compared to the DNA scaffold (~86 kDa) and AChE (280 kDa). Fractions from the main and second peak were collected and further characterized by native polyacrylamide gel electrophoresis (PAGE). Compared to the DNA scaffold, several bands with lower mobility were identified likely due to variable numbers of AChE (from 1 to 4) conjugated to the DNA scaffold (Fig. 2*E*). Bands that presumptively contain ACh nanosensors displayed overlapping fluorescence of pHAb and AF647, demonstrating structural integrity of ACh nanosensors (*SI Appendix*, Fig. S2). The purified

ACh nanosensors exhibited peak absorbances around 260 to 280 nm arising from the DNA and protein, 532 nm from pHAb fluorophores, and 647 nm from AF647 (Fig. 2*F*). To calculate the ratio of conjugated AChE and BTX to DNA scaffold, we estimated concentration of BTX-AF647 ([BTX]) by measuring the absorbance at its maximum absorbance of 652 nm. We then estimated extinction coefficients (i.e., ε) of the DNA scaffold, AChE, and BTX at 260 and 280 nm by measuring the absorbance of pure DNA or protein samples.

$$\frac{A_{260}}{b} = \varepsilon_{260}^{DNA} \times [DNA] + \varepsilon_{260}^{AChE} \times [AChE] + \varepsilon_{260}^{BTX} \times [BTX]. \quad [1]$$

$$\frac{A_{280}}{b} = \varepsilon_{280}^{DNA} \times [DNA] + \varepsilon_{280}^{AChE} \times [AChE] + \varepsilon_{280}^{BTX} \times [BTX]. \quad [2]$$

Based on the above Beer–Lambert Law calculations, the conjugation ratios of AChE, BTX, and pHAb to DNA scaffold were determined to be 2.86, 1.70, and 3.85 (Fig. 2*G*). The conjugation efficiency of BTX and pHAb reached 85 and 96%, respectively. The slightly lower conjugation efficiency of AChE (i.e., 71%) may be attributed to steric hindrance during the DNA–enzyme reaction. The agreement between measured and designed ratios supports the high predictability of the DNA nanostructure self-assembly. Compared to our previous version with an estimated size of ~130 nm (24), the current ACh nanosensor had an overall size of 10 to 20 nm confirmed by both structural simulations and atomic force microscopy (*SI Appendix*, Fig. S3). It is worth noting that due to the inherent flexibility of DNA structures (36, 37), the hydrodynamic size of ACh nanosensor is even smaller, potentially making it compatible with small biological features such as the synaptic cleft.

ACh Nanosensors in SMG. The SMG parasympathetic ganglia that innervate the salivary glands was chosen to validate our nanosensor because 1) it is relatively accessible for optical imaging, 2) it is a well-established model of ACh release, and 3) the SMG contains large neurons with no dendrites that are mainly innervated by a single cholinergic fiber that activate nicotinic ACh receptors on the cell soma (38, 39). To expose the SMG, we adapted a protocol for time-lapse imaging of interneuronal synapses in SMG from previous literature (28, 40). We first made a small incision on the neck and then placed an insulated metal platform under the salivary ducts to lift and stabilize the SMG to be imaged with a water-immersion objective. The flat metallic support greatly reduced respiration-induced movements which would cause defocusing and signal fluctuations during imaging. Several SMGs can be identified along the salivary ducts by removing the nearby connective tissues (*SI Appendix*, Fig. S4 *A* and *B*). Ex vivo staining of freshly isolated SMG with BTX-AF647 showed the expected punctate staining pattern across the ganglion, confirming expression of nicotinic ACh receptors in SMG neurons (*SI Appendix*, Fig. S5).

ACh nanosensors were administered in vivo to the SMG by local microinjection. Fig. 3*A* shows the setup for microinjection: a pulled glass needle filled with nanosensors was used for injection by rapid filling of extracellular space in the SMG, which can be observed as fluorescent rings surrounding each ganglion cell after injection (Movie S1). Injection was performed using a widefield microscope with low-magnification (4× objective) and dual imaging of pHAb and AF647 channels (Fig. 3*A*) (detailed in *Materials and Methods*). Some ACh nanosensors were found along the nerve tract that entered and exited the SMG (*SI Appendix*, Fig. S4*C*). After extensive buffer rinsing, a significant amount of ACh nanosensors remained inside the SMG (Fig. 3*B*). The stability test confirmed that the ACh nanosensors maintained their structural integrity and functional abilities within the tissue across a 5 h experimental length, as evidenced by the overlap in fluorescence of BTX-AF647 and pHAb and changes in the fluorescence intensity of pHAb, demonstrating rapidly responsive AChE activity (*SI Appendix*, Fig. S4 *D* and *E*). In contrast, DNA structures that did not have the AChE and targeting ligands (i.e., BTX) were barely visible inside the tissue (Fig. 3*C*). Confocal microscopy further confirmed that the punctate staining pattern of AF647 and pHAb were primarily localized on the neuronal cell soma (Fig. 3*D*). The consistent staining patterns of ACh nanosensors in the SMG in vivo along with the ex vivo staining of the SMG with BTX-AF647 (*SI Appendix*, Fig. S5) support that ACh nanosensors bind to nicotinic ACh receptors via conjugated BTX. Compared with BTX labeling, the confocal imaging of nanosensor-labeled tissue showed less membrane labeling probably due to the lower mobility of the nanosensor in the extracellular matrix.

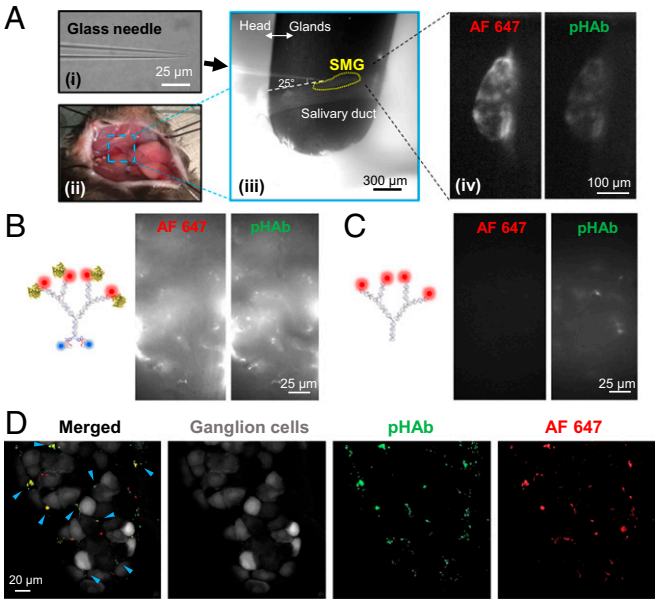

Fig. 3. ACh nanosensors in SMG. (*A*) Microinjection of the ACh nanosensors into an SMG of a living mouse via (i) a glass needle. (Scale bar, 25 μm.) (ii and iii) The SMG on a salivary duct was exposed by surgical incision and moving the salivary gland away from the duct. (Scale bar for iii, 300 μm.) (iv) ACh nanosensor–stained SMG observed under 4× objective. (Scale bar, 100 μm.) SMG stained by (*B*) ACh nanosensors and (*C*) DNA structures that do not have BTX-AF647 and AChE were washed away after injection. (Scale bar, 25 μm.) (*D*) Confocal imaging of the nanosensor-stained SMG in a ChAT(BAC)-eGFP transgenic mouse after removal and fixation. Gray: ganglion cells; green: pHAb fluorophores; and red: AF647 fluorophores. Yellow (highlighted by blue arrows) indicates the overlap of the pHAb and AF647 fluorophores. (Scale bar, 20 μm.) Image credit: J.X. (Northeastern University, Boston, MA).

Ex Vivo Calibration of the ACh Nanosensors. We next measured the response of the ACh nanosensors ex vivo using exogenous ACh to build a calibration curve. The SMG was microinjected in vivo with nanosensors, isolated, and then imaged by positioning the SMG under a metal harp in a bath imaging chamber (Fig. 4*A*) as we changed the ACh concentration in the surrounding bath solution. Qualitatively, we observed a significant rise in fluorescence intensity as the ACh concentration increased stepwise from 0.71 nM to 7.14 mM (Movie S2), as predicted. *SI Appendix*, Fig. S6*A* indicates the initial nanosensor response to ACh addition was within 0.55 s, the minimum sampling time used in our experiment. We believe the enzymatic response is much faster than this value, which inherently includes the solution addition and mixing time as well as the enzymatic response. The rapid response of ACh

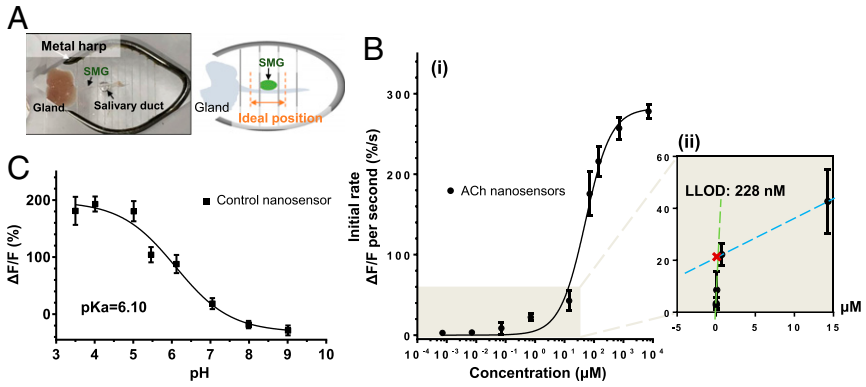

Fig. 4. Ex vivo calibration of ACh nanosensors. (*A*) The setup for the ex vivo calibration of the control and ACh nanosensors. The SMG was isolated immediately following the microinjection of the nanosensors into the tissue and later positioned under a metal harp in a bath imaging chamber for imaging. (*B*) The initial rates of the sensor response to exogenous ACh solutions at different concentrations. The sigmoidal nonlinear curve was fit by the Michaelis–Menten equation with the constants K_m= 49.24 ± 5.84 μM, V_{max}=281.00 ± 7.14%/s, and R^2 = 0.9811. (ii) An expanded view of the region denoted in gray in i. The data in the lower concentration range (up to 14.28 μM) were grouped into two linear regions (i.e., green and blue lines); the two dashed lines intersect at [ACh] = 228 nM, corresponding to the LLOD. (*C*) Fluorescence change of control nanosensors under different pH levels ranging from 3.5 to 9. The error bars denote SD resulting from triplicate experiments (three mice) in both *B* and *C*. Image credit: H.Y. (Northeastern University, Boston, MA).

nanosensors indicates that enzymatic kinetics is not a limiting factor of sensor response. The initial rates of change in pHAb fluorescence intensity were fitted and analyzed by the Michaelis–Menten equation (Fig. 4*B*). From the curve, we see that the half-maximum response (EC_{50}) to ACh was 49.24 ± 5.84 μM and upper limit of detection was 358.01 μM. To determine the lower limit of detection (LLOD), experimental data in the lower concentration range (i.e., 0.71 nM to 14.28 μM) was grouped into two linear regions with the two regression lines crossing at a value of [ACh] = 228 nM. The theoretical nanosensor response at LLOD of 0.72% in unit recording time (i.e., increase rate 1.3%/s is derived from Michaelis–Menten equation and the recording internal is 0.55 s) was significantly higher than the background noise (i.e., 0.088% ± 0.039%). The signal-to-noise ratio of the LLOD was 8.18, which provided an estimate of [ACh] = 228 nM as the LLOD. It has been estimated that the concentration of ACh ranges from low- to mid-micromolar in vivo, which lies within the detection range of our ACh nanosensor (30, 41, 42). Concerns may arise regarding whether the ACh nanosensor's response can be influenced by the amount of nanosensors present in the SMG. Thus, we separately normalized the initial rate (i.e., V_{sensor}, ΔF/F per second, and %/s) with the unit initial rate (i.e., $V_{unit\ sensor}$, ΔF/F per second per nanosensor, %/(s · nM)). Specifically, the nanosensor concentration in the region of interest (ROI) was calculated based on the fluorescence intensity of AF647 (internal standard) via a linear calibration curve derived from ACh nanosensors of known concentrations. The normalized unit initial rate $V_{unit\ sensor}$ was obtained by dividing the original V_{sensor} in Fig. 4*B* by the as-calculated nanosensor concentration (nM). The $V_{unit\ sensor}$–[ACh] relationship was further analyzed by the Michaelis–Menten equation (*SI Appendix*, Fig. S6*B*), which showed an almost identical curve to Fig. 4*B* with an EC_{50} value of 50.35 ± 6.76 μM. A double reciprocal plot was obtained from the fitted Michaelis–Menten equation as Eq. 3 and used to quantify ACh concentrations in the in vivo experiments.

$$\frac{1}{V_{unit\ sensor}} = 126.41 \times \frac{1}{[ACh]} + 2.499. \quad [3]$$

As with many optical probes for cellular studies (43–45), our nanosensors are dependent on pH and could potentially respond to endogenous changes in pH not associated with the sensing mechanism. As a control for measuring pH, we fabricated a nanosensor with only pHAb fluorophores and BTX on the DNA scaffold (no enzyme, termed "control nanosensor"). We calibrated the response of the control nanosensor toward varying pH levels in an ex vivo tissue preparation. The signal change from pH 7 to 5 ranged from 18.50 ± 9.74% to 180.43 ± 17.67% with a pK_a of 6.10 (Fig. 4*C*), in accordance with the pK_a value of 6.2 representing free pHAb fluorophores (*SI Appendix*, Fig. S7*A*). The large signal change in mildly acidic conditions is a property that favors detection of ACh with our proposed sensing mechanism that generates a localized acidic environment in the vicinity of the enzymes.

In Vivo Imaging of ACh Release. ACh nanosensors were microinjected into the SMG as previously shown in Fig. 3*A*. Electrical stimulation of the lingual nerve was performed (3 V, 10 Hz, 10 ms duration, and 100 pulses) to evoke release of ACh into the SMG (Fig. 5*A* and *SI Appendix*, Fig. S4 *A* and *B*) (46). Upon the stimulation of the lingual nerve, fluorescence intensity increased 3.7% by 15 s with initial velocity of V_{sensor} = 0.294 ± 0.116%/s, which slowly recovered to baseline within 2 min (Fig. 5*B*). Stimulation evoked a steady increase in signal over ∼15 s, likely indicating persistent presynaptic firing. In contrast, we observed a minimal response when control nanosensors were tested, demonstrating that the influence of intrinsic pH fluctuation is negligible. However, upon stimulation with a higher 10 V voltage, control nanosensors responded to ∼50% of the ACh nanosensor signal intensity (*SI Appendix*, Fig. S8), suggesting higher stimulation induces a pH change, possibly due to cellular damage or endogenous enzyme. Varying the electrode stimulation parameters led to a dose-dependent ACh nanosensor response (V_{sensor}) with 3 V stimulation increasing 0.1886%/s, 5 V increasing 3.24%/s, and 10 V increasing 11.35%/s, all collected at the same ROI in the ganglia (Fig. 5*C*). Similarly, increasing the number of pulses also led to a higher ACh nanosensor response (Fig. 5*D*). Reversibility of the sensor was demonstrated by three repeated stimulations (10 V, 10 Hz, 10 ms duration, and 10 pulses), showing repeatable rates of 0.436%/s, 0.417%/s, and 0.431%/s in sequence (0.428 ± 0.010%/s, Fig. 5*E*), which was confirmed with in vitro experiments (*SI Appendix*, Fig. S7*B*).

Next, we quantified ACh concentration using the established calibration curve. In Fig. 5*C*, the $V_{unit\ sensor}$ values for electrical stimulation of 3 V, 5 V, and 10 V were 0.0214%/(nM · s), 0.0711%/(nM · s), and 0.2448%/(nM · s), respectively. Using Eq. 3, we estimated the endogenous ACh concentrations to be 2.75 μM at 3 V, 10.49 μM at 5 V, and 76.51 μM at 10 V. Note that calculated values are above the LLOD with a high signal-to-noise ratio.

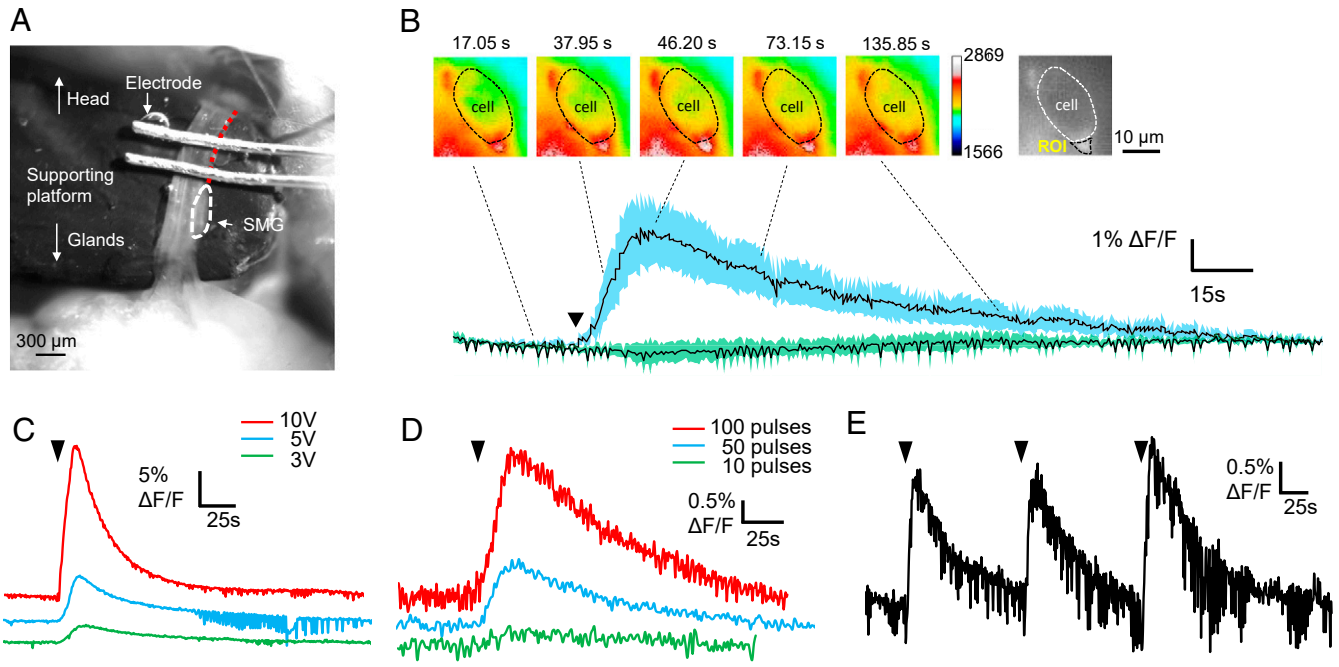

Fig. 5. In vivo imaging of ACh release. (*A*) Bright-field image showing the setup of electrical stimulation. The red dashed line indicates segments of nerves being stimulated. (Scale bar, 300 μm.) (*B*) ΔF/F from the pHAb channel in response to electrical stimulation (indicated by the black arrow). The panel of time-lapse fluorescence images display a typical ACh nanosensor–stained, single-ganglion cell used for plotting. The data were averaged from three independent experiments ($n = 3$ mice). The error bars are illustrated as blue and green areas for ACh nanosensors and control nanosensors, respectively. (Scale bar, 10 μm.) Stimulation parameters: 3 V, 10 Hz, 10 ms duration, and 100 pulses. (*C* and *D*) Dose-dependent response and in vivo reversibility of ACh nanosensors. Each graph was derived from changing or keeping the electrical stimulation "dose" on a single animal. (*C*) Plot of ΔF/F in the same ROI in response to the electrical stimulation with different voltage amplitudes (i.e., 3 V, 5 V, and 10 V). Other stimulation parameters: 10 Hz, 10 ms duration, and 100 pulses. (*D*) Plot of ΔF/F in the same ROI in response to the electrical stimulation with different numbers of pulses (i.e., 100, 50, and 10). Other stimulation parameters: 10 Hz, 10 ms duration, and 3 V. (*E*) Plot of ΔF/F in the same ROI of three repeated electrical stimulations. Stimulation parameters: 10 V, 10 Hz, 10 ms duration, and 10 pulses. Note that *y*-axis scale in *D* and *E* is different from *C*.

As a second confirmation of the response to ACh, an anticholinergic drug, vesamicol, was introduced to temporarily block the release of ACh. Vesamicol inhibits ACh release by inhibiting ACh uptake into synaptic vesicles in presynaptic neurons (47). We incubated the nanosensor-stained SMG with vesamicol for 10 min and recorded the sensor's response with electrical stimulation at 3 V. We then washed away the vesamicol and stimulated the lingual nerve under the same stimulation conditions. The ACh nanosensors reported only 17% response with the drug compared to after the drug was washed from the sample (Fig. 6 *A* and *B*). Four independent inhibitor treatments affirmed that vesamicol can considerably suppress ACh nanosensors' readout by an average of 76.59 ± 11.34% (Fig. 6*C*), serving as a strong evidence that the ACh nanosensor signal indeed stems from endogenous ACh release.

ACh Nanosensor Response Reflects Physiological ACh Propagation. We observed that lingual nerve stimulation induced a complex

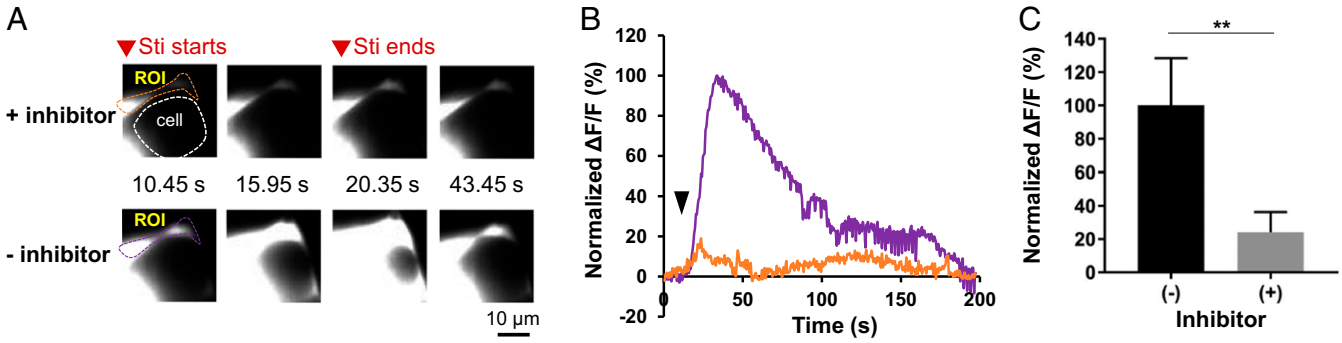

Fig. 6. ACh nanosensor's response to the ACh release with or without vesamicol, an ACh inhibitor. (*A*) Time-lapse fluorescence images showing the real-time fluorescence readout before and after washing away the vesamicol. (Scale bar, 10 μm.) (*B*) ΔF/F of fluorescence intensity from pHAb channel plotted from ROI (purple and orange dashed line) in *A*. (*C*) The peak value of ACh nanosensor response from four independent inhibitor experiments. By the paired *t* test, a significant difference (**$P < 0.01$) was found between the vesamicol treated and untreated groups for all four trials. Fluorescence intensity was normalized at the maximum value in *B* and *C*. Stimulation parameters for drug experiments: 3 V, 10 Hz, and 10 ms duration, 100 pulses. The black triangles indicate the start of the stimulation.

spatiotemporal response across the SMG. To quantify this complex response, we applied the AQuA software, which can accurately quantify irregular fluorescence dynamics (32). In AQuA, coordinated fluorescence dynamics are classified as "events," and these events vary in area, duration, amplitude, and propagation. As such, no predetermined ROIs are selected for a less-biased method of image analysis. AQuA is particularly powerful in the analysis of fluorescence dynamics that are irregular, heterogeneous, and/or propagative. Here, we used AQuA to analyze the fluctuations in intensity of the individual pixels within SMG. To compare the temporal ACh nanosensor response calculation between AQuA to our original ROI-based analysis, we compared the fluorescence dynamics derived from AQuA software to the ROI-based analysis at the same regions that were automatically defined by AQuA software and found that they reported similar dynamics (*SI Appendix*, Fig. S9). It is worth noting that control nanosensors change less than 4% under 8 V stimulation (*SI Appendix*, Fig. S10, which indicates that there are minimal changes in physiological pH in this system). We next applied AQuA to quantify the spatial propagation of the fluorescent signal across the ganglion. Since the SMG is a well-established model of ACh release (38, 39) and we stimulated preganglionic axons based on established methods (28, 40), we expected to observe rostral-to-caudal ACh transmission. The spatiotemporal AQuA analysis of nanosensor response following 8 V stimulation across the SMG validated our prediction (Fig. 7*A* and Movie S3). The rostral-most region started to increase fluorescence at 13.20 and 2.75 s after the start of 10 s stimulation and peaked at t = 22.0 s, 1.65 s after the last stimulation. The signal propagated caudally by t = 13.75 and 15.40 s and further traveled laterally at t = 15.95 s, around 2 s behind the rostral-most region (Fig. 7*A* and *SI Appendix*, Fig. S11). The rapid onset response of ACh nanosensor is consistent with in vitro kinetics (*SI Appendix*, Fig. S6*A*). The decay of fluorescence intensity of the most caudal region begins at t = 44.55 and 24.2 s after the last stimulation (Fig. 7*B*). The long temporal release of ACh may be due to a combination of preganglionic projections into the SMG as well as intrinsic connections between SMG neurons. Interaxonal connections between preganglionic neurons have been observed as well as neuronal connections between postsynaptic SMG neurons. Slow postsynaptic potentials on the order of seconds have also been observed, which may be a mechanism related to the continuous ACh release we observed here (48). All evoked nanosensor responses in Fig. 7*A* climbed to the peak around ~10 to 15 s, an observation consistent with Fig. 5 *B*–*E*. We also conducted the same analysis with a lower stimulation voltage of 3 V for three independent experiments and observed similar rostral-to-caudal propagation directionality (Movie S4 and *SI Appendix*, Fig. S12). The overall lower amplitude in signal output under 3 V stimulation compared to 8 V is also consistent with the dose-dependent sensor response in Fig. 5*C*. It is worth noting that previous work focused more on single-cell recording (49) and ion-channel (50) and receptor recycling (51) of ganglion cells; we instead demonstrated the spatial direction of ACh transmission in the SMG.

Discussion

We envision our technology is a great addition to the toolbox of detecting neurotransmission in CNS and PNS. Firstly, we developed the DNA-based enzymatic nanosensor based on a bottom-up modular design and assembly process. The DNA scaffold empowers the ACh nanosensor versatility and can be easily repurposed for other applications or imaging in different regions of the body and brain. In this work, the DNA scaffold plays a key role in the accurate positioning of the functional motifs, AChE and pHAb, in close proximity for sensitive detection of the pH drop caused by ACh hydrolysis, meanwhile keeping the overall size of the sensor to be 10 to 20 nm to facilitate localization within complex, heterogeneous tissues. We can achieve either blueshift or redshift in imaging wavelength by substituting pHAb with other pH-sensitive fluorophores. Moreover, pHAb fluorophores are also compatible with two-photon imaging (*SI Appendix*, Fig. S13), which allows deep-tissue imaging and efficient reduction of background noise, a landmark advantage for brain imaging as well as deeply encapsulated tissues in the PNS. The AChE and pH-sensitive fluorophores can be substituted with other functional motifs to target other neurotransmitters (e.g., tyrosinase and oxygen-sensitive fluorophores for sensing dopamine) (52).

Additionally, we chose nicotinic ACh receptors as the binding target because it is used broadly across the body including the CNS and sympathetic, parasympathetic, and somatic PNS and because of its well-studied binding affinity to BTX (28, 35). Successful employment of the same receptors as the targeting region is also demonstrated in other genetically modified sensors (53). For organs/tissues with low expression of nicotinic ACh receptors, the targeting ligand (BTX), can be replaced by other biomolecules for targeting other receptors of interest (such as muscarinic ACh receptors). As with any measurement tool, concerns may arise regarding whether the tool itself distorts the environment. Namely,

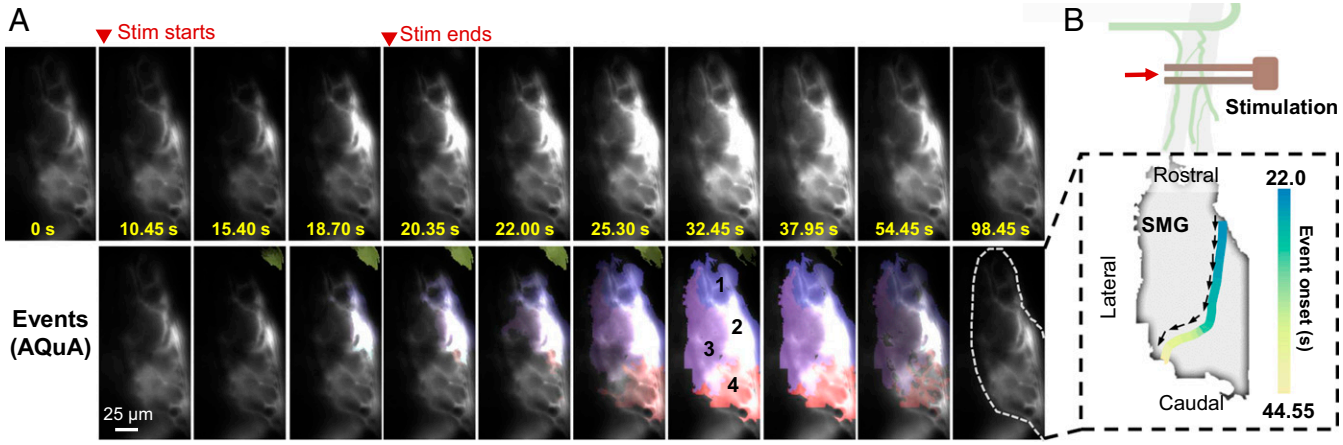

Fig. 7. AQuA program resolves the ACh propagation directionality. (*A*) Time-lapse images (*Upper*) exhibit a whole SMG injected with the ACh nanosensors under electrical stimulation. Bottom shows the same series of images with the AQuA-detected events. Different colors indicate the different events that AQuA detected. The order of onset time of four areas are labeled as 1, 2, 3, and 4. (Scale bar, 25 μm.) (*B*) In vivo ACh transmission propagates with specific directionality in *A*. Time scale indicates the time that each area reaches its maximum fluorescence intensity. Stimulation parameters: 8 V, 10 Hz, and 10 ms duration, 100 pulses.

binding between BTX and ACh receptors could block normal ACh signal transmission and negatively affect or harm the imaging subject. We anticipate that our ACh nanosensors have a limited impact on neurotransmission because a substantial number of ACh receptors in the synapses would still remain available. Based on the literature, there is about a 50% occupancy of the ligand BTX to alpha-7 nicotinic ACh receptors in the SMG (51). The availability of additional ACh receptors is also supported by the regeneration of membrane-bound ACh receptors in SMG via continuously removing/inserting receptors from/to the plasma membrane (51). We observed fewer nanosensors attached to the SMG than with BTX alone (Fig. 3 and *SI Appendix*, Fig. S5), which suggests that more than 50% of receptors are unoccupied. Thus, although some degree of interference may be inevitable, we anticipate that synaptic transmission is still occurring.

A major accomplishment in this work is the successful imaging of endogenous ACh release in the SMG and the tracing of ACh transmission on the tissue level. Two principal factors support that the detected signal originates from endogenously released ACh: 1) electrical pulses trigger dose-dependent and reversible responses from the ACh nanosensor and 2) the signal can be significantly recovered after removal of vesamicol, a presynaptic ACh inhibitor. The rapid onset response of ACh nanosensor in vivo is consistent with in vitro kinetics and not significantly behind the stimulation. The gradual decrease in response of ACh nanosensor stems from 1) reaction time for AChE to hydrolyze ACh induced by 10 s stimulation, and 2) the slow neutralization process between narrow gaps inside SMG, and extracellular buffering system. It is worth noting that it also takes genetically encoded ACh sensors 40 s to return to the baseline in slices of medial entorhinal cortex after 10 s stimulation (20 pluses at 2 Hz) (6). The "off" time of ACh nanosensor is comparable to latest genetically encoded sensors. The quantification of endogenously released ACh is achieved via establishing an ex vivo calibration curve. As reported, ACh concentrations lie in the range of low to midmicromolar predominantly in the CNS, whereas few estimates have been made in the PNS except for the neuromuscular junctions. In contrast to single-point detection tools, such as electrodes which are ineffective against spatial mapping, the benefit to an imaging probe is the ability to attain spatial information in addition to temporal, especially when the signal is irregular and propagative. Our data provides insights into measuring ACh concentration in the PNS and spatial mapping of ACh signal transmission on the tissue level, a significant advance in resolving cholinergic transmission in the PNS. The propagation directionality derived from advanced algorithmic image processing facilitates spatiotemporal mapping of cholinergic transmission. The algorithm can be expanded to three-dimensional imaging of neurotransmitter dynamics using confocal, two-photon, and light sheet microscopy (32). With the evolution in machine learning–based image processing and advancement in high-resolution volumetric imaging, we envision this sensing platform will serve as a powerful tool to elucidate the underlying mechanisms in cholinergic circuitry.

We designed our ACh nanosensors for imaging ACh release in the PNS and found that the exogenous delivery of ACh nanosensors (e.g., microinjection) into the SMG was relatively simple. Our goal is to extend this technique to new anatomical areas in a variety of animals, even human tissue. Moreover, our ACh nanosensors can be easily adapted to established live imaging protocols for different organs/tissues for a broad range of physiological research groups interested in neurotransmission. Our ACh nanosensor will expand the analytical toolbox for mapping ACh transmission in real time in the PNS and CNS in different species, enabling the elucidation of fundamental and disease-relevant neurological pathways.

As with any tool, there are issues to be addressed in future designs. First, the DNA scaffold was designed for the environment of the SMG and could degrade in the presence of degradative enzymes in the bloodstream. The next stage of development will focus on the scaffold by using enzyme-resistant nucleotides or shielding the sensor with polyethylene glycol (PEG). The fluorophores could be substituted to minimize photobleaching for longer-term monitoring of ACh release. By developing imaging protocols to include a custom optical setup for intravital imaging and tissue stabilizers to suppress contraction in a local area, the sensor could have impact in cardiac imaging (54), even of larger animals. In addition, better labeling techniques could ensure that all cells are labeled and no synaptic transmission information is lost. Future directions may include comparison of quantitative neuron activity from other methodologies with our ACh nanosensors on the same organ/tissue. In summary, we show a biochemical nanosensor that rapidly responds to endogenous ACh release in a dose-dependent and reversible manner and exhibits significantly improved spatial flexibility that enables mapping of ACh signal transmission on the whole-tissue level. This work sheds light on an imaging modality that consolidates sensitivity, temporal and spatial resolution, and comprehensively resolves ACh transmission in the PNS.

Materials and Methods

Design and Fabrication of the ACh Nanosensor. We designed the size of the scaffold based on a trade-off between diffusion through tissue and optimal signal. A branched dendritic structure with a focal point was chosen based on previous studies (24) and the redundancy in attachment sites because yield during conjugation is less than 100% (Fig. 2*G*). Since a decrease in the number of conjugated enzymes significantly lowers the relative activity of the sensor (24) and because AChE has an ellipsoidal shape with dimensions of ~45Å × 60Å × 65Å, we accommodated up to four enzymes and four fluorophores on a single sensor to maximize sensor response while maintaining an overall size under 20 nm. In addition to the sensing components, we also needed a targeting ligand, therefore necessitating a DNA dendrimer of five branches to provide 10 anchoring points so that at least one targeting ligand molecules would be present. Next, we designed each arm of the scaffold to be 20 base pairs (~6 nm), with an estimated free energy of folding of −154.7 kCal/mol (calculated by RNAfold) (55), which minimizes the steric hindrance of the enzymes (~4 to 6 nm) attached to the DNA scaffold while maintaining the overall sensor size under 20 nm. The structure of the DNA scaffold was designed to accommodate four AChE enzymes (electrophorus electricus, Millipore-Sigma), four pHAb fluorophores (Amine-reactive, Promega), and two BTX molecules (AF647 conjugated, Thermo Fisher). Preliminary sequences were obtained by a random sequence generator (56) to anneal into a dendritic secondary structure with four branches and a focal point as confirmed by Nanoengineer-1 program (Molecular Dynamics Studio). ssDNA oligonucleotides with amine or thiol functional groups were purchased from Sigma. Before annealing the DNA scaffold, pHAb dyes were conjugated to DNA strands (i.e., L2, L3, and L4) via N-hydroxysuccinimide (NHS) ester reactions (*SI Appendix*, Fig. S2). The same reaction was also employed to modify two amine groups in strands L1 and L5 with tetrazine groups via tetrazine linkers (Tetrazine–PEG5–NHS ester, Broadpharm) (*SI Appendix*, Fig. S2), which were later used to conjugate BTX. Reactions were conducted in 0.1 M $NaHCO_3$ solution (pH = ~8.1 to 8.2) at a DNA concentration of 100 to 150 μM. Modified single strands (L1 to L5) were first separated from excess pHAb dyes and tetrazine cross-linkers by two rounds of ethanol extraction and further purified by illustra NAP-10 columns (GE Health) via gel filtration, followed by overnight lyophilization (Labconco).

The DNA scaffold was self-assembled by incubating five DNA oligonucleotides following a temperature gradient from 95 to 4 °C for 6 h in a thermocycler (Mastercycler nexus ×2, Eppendorf) in Tris– ethylenediaminetetraacetic acid (EDTA) buffer (TE buffer, 10 mM Tris and 1 mM EDTA). Misfolded DNA scaffolds were removed by a size-exclusion column (Superdex 200 increase 10/300 GL column, GE Health) via HPLC (Infinity 1260, Agilent) using phosphate buffer (500 mM NaCl) as the eluent (*SI Appendix*, Fig. S14*A*). The correct fraction was collected and resuspended in TE buffer via buffer exchange. The fully assembled DNA scaffold can be stored in a −20 °C freezer for up to 6 mo. Two proteins were attached to the DNA scaffold after the annealing process. Before enzyme modification, we first employed size-exclusion HPLC to purify AChE since the commercially available AChE (from eel extract) is not of 100% purity (*SI Appendix*, Fig. S14*B*). The correct fraction was collected for further modification with maleimide functional groups. For protein functionalization, 30 to 50 μM of AChE was swirled with maleimide linkers (maleimide–PEG12–NHS

ester, Pierce SM(PEG)$_{12}$ Thermo Scientific) for 2 h before being purified by 100 k Amicon centrifugal filter five times. BTX was maintained at ~500 μM when reacting with TCO linker (TCO–PEG$_4$–NHS ester, Click Chemistry Tools). In the aforementioned protein–linker reactions, either AChE and BTX solution was incubated with corresponding cross-linkers at a molar ratio of 1 : 20 to keep the balance between linkage efficiency and protein activity. Assembled DNA scaffolds were pretreated with tris(2-carboxyethyl)phosphine (TCEP) for 1.5 h at room temperature to cleave the disulfide bonds and then removed from excess TCEP via Amicon centrifugal filters (30 k cutoff) prior to enzyme conjugation. Maleimide-functionalized AChE was later vortexed with the DNA scaffold at a molar ratio of 5:1 for 2 h. Afterward, TCO-functionalized BTX was added to the reaction mixture at a BTX to DNA molar ratio of 20:1, allowing a TCO–tetrazine ligation reaction between BTX and the DNA scaffold for another 2 h. The unreacted thiol groups were later capped by ethylmaleimide (Fisher Chemical). The final reaction mixture was vortexed for 30 min before transferring to a 4 °C fridge for overnight incubation.

After protein–DNA conjugation, ACh nanosensors that contain DNA scaffold, AChE, and BTX were separated from other impurities by a size-exclusion column (Superdex 200 increase 10/300 GL column, GE Health) via HPLC (Infinity 1260, Agilent). The elution solution was 0.15 M phosphate buffer with NaCl concentration of 500 mM. Three absorbance signals (i.e., 260 and 280 nm for DNA and protein absorbance and 652 nm for AF647) and one fluorescence signal (i.e., Ex = 532 nm and Em = 560 nm for pHAb) were monitored during elution. After purification, ACh nanosensors were concentrated by 100 k Amicon ultra centrifugal filters and then aliquoted for long-term storage at −20 °C. The typical concentration of ACh nanosensors was around 2 to 4 μM in each aliquot.

Enzyme Assay. The enzymatic activity of AChE was calculated based on the Ellman Esterase Assay (57). The substrate solution was prepared by mixing 100 μL of Ellman's reagent (DTNB, 5,5′-dithio-bis-[2-nitrobenzoic acid], 3.96 mg/mL), 40 μL of 75 mM acetylthiocholine iodide (Millipore-Sigma), and 3 mL 100 mM sodium phosphate buffer (pH = 7.0 to 8.0). A total of 200 μL substrate solution was first added to a 96-well plate. After 40 μL AChE/ACh nanosensor solution was quickly added, the kinetic absorbance of the mixture solution was immediately recorded by SpectraMax M3 plate reader (Molecular Devices) at the wavelength of 412 nm. The time that the solution reached the peak plateau was used for calculation of enzymatic activity via Eq. 4.

$$Enzyme\ activity(U/mg) = \frac{Amount\ of\ acetylthiocholineiodide(\mu Mole)}{Amount\ of\ AChE(mg) \times Reaction\ time(min)}. \quad [4]$$

Characterization of ACh Nanosensors. The ultraviolet–visible spectroscopy spectrum of DNA scaffold/sensors was measured by a NanoDrop 2000c Spectrophotometer (Thermo Scientific). Native PAGE was conducted to characterize DNA nanostructures by using 4% tris/borate/EDTA (TBE) gel and 1× TBE buffer at a constant voltage of 200 V (electrophoresis system Thermo Scientific) in an ice water bath. The in vitro reversibility test of ACh nanosensors was conducted in a slotted imaging bath (RC-21BRFS, Warner Instrument). The sensors were carefully introduced into a microdialysis hollow fiber (13 kDa, Spectrum Laboratories) via capillary action. The two ends of the dialysis tube were then sealed by super glue and quickly attached to the glass bottom of the flow chamber. After the cap of the chamber was closed, 10 mL Ringer buffer was slowly injected into the chamber to prevent any air bubbles. The tubing was then connected to a peristaltic pump (Fisherbrand) and waste bottle. The chamber was carefully placed on the confocal imaging stage (LSM 800, Zeiss) under a 20× objective. An ACh solution of 100 μM (acetylcholine chloride, Millipore-Sigma) was injected into the chamber while the imaging started. After 2 min of imaging, the remaining ACh was washed away by Ringer's buffer to allow the sensor to recover to the initial state. The injection of ACh was repeated five times.

Atomic force microscope (AFM) measurement was conducted following literature precedent (58). All buffers were freshly prepared and filtered through 0.22 μm filters on the experiment day. In short, freshly cleaved mica (Ted Pella) was incubated with 20 μL of 100 mM $NiCl_2$ for 1 min and rinsed with 50 mL ultrapure water. The mica was then quickly dried by filter paper, immediately followed by deposition of 20 μL of 1 nM ACh nanosensors in deposition buffer [10 mM HEPES (4-(2-hydroxyethyl)-1-piperazineethanesulfonic acid, pH 7.5) and 10 mM $MgCl_2$ + 25 mM KCl]. After 2 s, the mica surface was gentle rinsed by ~10 mL deposition buffer and 2 mL imaging buffer [10 mM HEPES (pH 7.5) and 10 mM $NiCl_2$ + 25 mM KCl], in sequence. The same imaging buffer was also deposited onto the microscope tip. Samples were imaged in "ScanAsyst mode in fluid" using a Dimension FastScan microscope with PEAKFORCE-HiRs-F-A tips (Bruker Corporation) (59).

Animal Preparation and Imaging. Adult male and female C57BL/6J (RRID: IMSR_JAX: 000664) and ChATBAC-eGFP (RRID: IMSR_JAX: 007902) mice between the ages of 4 to 8 wk old were obtained from the Jackson Laboratory. All mice were maintained under the conditions mandated by Northeastern University's Division of Laboratory Animal Medicine. All animal procedures were approved by the Institutional Animal Care and Use Committee at Northeastern University and were in accordance with the NIH guidelines. To better visualize the staining of the ACh nanosensors in the SMG, ChATBAC-eGFP mice that specifically express green fluorescent protein (GFP) in the cholinergic cells and presynaptic axons fibers were used. In all animal experiments, the mice were anesthetized by inhalation of 1.5 to 2% isoflurane and placed on a rodent heating pad (Braintree Scientific, Inc.) set at 37.7 °C. The mice were placed on their dorsal side under the dissection scope (Fisher Scientific) and after using depilatory cream, a small incision (about 1 cm) on the neck region was made, exposing the salivary glands. Fine tweezers (Fisher Scientific) were used to separate the salivary ducts from surrounding connective tissue. For live imaging, anesthetized mice were then carefully transferred to the stage of an upright fluorescence microscope (BX61WI, Olympus) for in vivo imaging experiments. W-VIEW GEMINI beam splitter (Hamamatsu) was incorporated into the optical path to image the pHAb and BTX-AF647 signals simultaneously. Images for quantifying in vivo ACh release were captured under a 60× water-immersion objective (numerical aperture = 1.0). The light source was Lambda LS Xenon Arc Lamp (300 W, Sutter Instrument). A neutral-density filter (25% transmission) was used to minimize photobleaching. In order to reduce crosstalk between the AF647 and pHAb channels, we chose the following optical sets (*SI Appendix*, Fig. S15): dual band bandpass filter (543/635 nm, Semrock) and multiedge beam splitter (560/659 nm, Semrock), bandpass filters (585/65 and 706/95 nm, Chroma) and longpass dichroic (635 nm, Semrock) mirror, and W-VIEW GEMINI beam splitter (Hamamatsu). *SI Appendix*, Fig. S16 exhibited a panel of time-lapse images from AF647 channel which were simultaneously recorded with the pHAb fluorescence in Fig. 7 and confirmed that there was no visible fluorescent increase during recording in AF647 channel. All data were corrected for photobleaching by first constructing a photobleaching curve using monoexponential decay. The original data were adjusted by first locating the measured fluorescence value on the photobleaching curve and then dividing by the number extracted from the curve.

Confocal microscopy was used for imaging the localization of ACh nanosensors/free BTX in freshly harvested SMG. For Z-stack imaging, 27 slices (17.41 μm) were captured under three fluorescence channels excited by lasers of 488, 514, and 633 nm at 1% laser power each.

In Vivo Microinjection of Nanosensors. The nanosensors or other DNA nanostructures were administered to the SMG of living mice via microinjection. After the initial dissection work as described previously, the salivary ducts were lifted up and supported by an insulated metal platform controlled by a micromanipulator for stabilization. A borosilicate glass tube with 1.0 mm/0.78 mm (outer diameter/inner diameter) was pulled using a P-97 micropipette puller (Sutter Instrument). Fig. 3*A* shows the tip of a pulled needle. The pulled glass needle was loaded with 4 μL of nanosensor solution, and it approached the submandibular ganglion from the proximal end at an angle of 25° using the Eppendorf InjectMan 4. Due to the use of a higher-magnification water-immersion lens, vacuum grease (Dow Corning) was carefully applied around the incision area to contain an aqueous solution without leakage. Afterward, the cavity created by the incision was filled with Ringer's solution and then using a 60× objective, the needle could precisely pierce into the SMG and enable nanosensor injection. The nanosensors were incubated within the SMG for 5 min, followed by washing with Ringer's buffer (~2 to 3 mL) for 10 min to remove unbound nanosensors.

Ex Vivo ACh Calibration. Anesthetized mice were euthanized by cervical dislocation immediately after the microinjection of nanosensors/control nanosensors. The SMG along with the salivary duct and the gland were quickly excised under a dissection scope. The dissected tissue was positioned within an open diamond bath imaging chamber (RC-26, Warner Instruments). The salivary duct was carefully stretched with an insect pin as a metal harp (Warner Instruments) was placed on top to suppress and stabilize the SMG (Fig. 4). After placing the chamber onto the microscope stage, 200 μL of freshly prepared Ringer's buffer (pH = 7.3 to 7.4) was added under the 60× water-immersion objective, followed by 500 μL injections of ACh solutions ranging in concentration from 0.001 μM to 10 mM. The final concentration of ACh was adjusted based on a dilution factor of 1.4. The entire experiment was performed using an Olympus BX61WI fluorescence microscope. After each measurement, the ACh solution was carefully removed using Kimwipes, followed by three rounds of washing with Ringer's buffer. The sample was then

immersed and incubated in the buffer for 10 min to enable the nanosensor to recover to baseline fluorescence signals. To acquire the calibration curve, the initial rates of change in pHAb fluorescence intensity were fit and analyzed by the Michaelis–Menten equation. Next, a linear fit region (14.71 to 164.82 μM) was determined from the tangent of EC_{50}, which represented the region with the highest rates of increase from the graph within 5% deviation from the Michaelis–Menten curve. The reported LLOD was found from the intersection of the two regression lines as [ACh] = 228 nM (Fig. 4*B*). For the calibration of control nanosensors, we repeated the same procedure with the exception of using citrate–phosphate buffers for pH < 6 and phosphate buffers for pH ≥ 7. Phosphate-buffered solution (pH = 7.3 to 7.4) was used for intermittent washings in between measurements of the control nanosensors. Error bars in Fig. 4 denote SD resulting from triplicate independent experiments (n = 3 mice). The analytical parameters of the sensor are also dependent on the imaging setup used for analysis and acquisition, so users would need to calibrate the sensors on their own system before use.

Electrical Stimulation. After microinjection of the nanosensors, a parallel bipolar electrode (FHC Inc.) was connected to a micromanipulator arm. Using an attached joystick module (Burleigh), the electrode was placed directly on the salivary duct, sitting above the SMG (closer to the lingual nerve). Electric pulses were generated by a MyoPacer field stimulator (IonOptix LLC) triggered by a pulse generator (Prizmatix). Bipolar pulses with an amplitude between 3 and 10 V, frequency of 10 Hz, pulse duration of 10 ms, and pulse number between 10 and 100 were delivered to the lingual nerves that innervate the SMG.

Drug Inhibition of ACh Release. After microinjection of the nanosensors, vesamicol (Millipore-Sigma, 100 μM in Ringer's buffer) was added dropwise to the neck cavity and incubated for 10 min to block the release of endogenous ACh. After each measurement was imaged and recorded, the drug solution was washed away with Ringer's buffer, and the neck region was bathed in Ringer's buffer for another 10 min to allow for the nanosensors to return to baseline fluorescence levels before recording the next measurement.

AQuA Analysis. The AQuA software (32) was used to accurately model and quantify the changes in intensity of nanosensor fluorescence in the SMG of a living mouse. Initially, a tagged image file format (TIFF) file of the experiment was uploaded with a set of preset values that described the frame rate, spatial resolution, and regions on the boundary of the video that were removed to apply motion correction. We defined the area to be analyzed by drawing a boundary around the entire SMG. The program determined and eliminated background noise from the video by increasing the intensity threshold scaling factor, and the signal was smoothed with a Gaussian filter. Events were determined by increasing the temporal cut threshold, removing all events below the intensity threshold. These events were then grouped together into "super events" based on the distance and time difference between the single events. AQuA analysis was conducted on three independent experiments (n = 3 mice). Dose-dependent stimulation was conducted on one mouse (3 and 8 V, shown in Fig. 7 and Movies S3 and S4) while the other two mice were stimulated at 3 V only (*SI Appendix*, Fig. S12).

Data Availability. Data have been deposited in https://discover.blackfynn.com/ (DOI: 10.26275/w027-cisv). Data associated with this study were collected as part of the Stimulating Peripheral Activity to Relieve Conditions (SPARC) program and are available through the SPARC Portal (RRID: SCR_017041) under a CC-BY 4.0 license.

ACKNOWLEDGMENTS. We thank Dr. Jeff Lichtman for early discussions on the imaging of the submandibular ganglion. We thank imaging support from the Northeastern University Institute for Chemical Imaging of Living Systems. We thank Dr. Guoxin Rong for assistance on two-photon imaging. We thank Mr. Alex Lovely for assistance on confocal imaging. We thank Dr. Jennifer Morales for early experimental discussion. We thank Dr. Qiong Wei for assistance on AFM. We thank Mr. Qizhong Wang for assistance on data analysis. This project was supported by NIH SPARC OT2OD024909. Development of AQuA program was supported by NIH R01NS099254 and NSF 1604544.

1. T. H. Ferreira-Vieira, I. M. Guimaraes, F. R. Silva, F. M. Ribeiro, Alzheimer's disease: Targeting the cholinergic system. *Curr. Neuropharmacol.* **14**, 101–115 (2016).
2. S. Perez-Lloret, F. J. Barrantes, Deficits in cholinergic neurotransmission and their clinical correlates in Parkinson's disease. *NPJ Parkinsons Dis.* **2**, 1–12 (2016).
3. A. Evoli, Myasthenia gravis: New developments in research and treatment. *Curr. Opin. Neurol.* **30**, 464–470 (2017).
4. T. Pradhan *et al.*, Chemical sensing of neurotransmitters. *Chem. Soc. Rev.* **43**, 4684–4713 (2014).
5. A. V. Leopold, D. M. Shcherbakova, V. V. Verkhusha, Fluorescent biosensors for neurotransmission and neuromodulation: Engineering and applications. *Front. Cell. Neurosci.* **13**, 474 (2019).
6. M. Jing *et al.*, A genetically encoded fluorescent acetylcholine indicator for in vitro and in vivo studies. *Nat. Biotechnol.* **36**, 726–737 (2018).
7. M. Jing *et al.*, An optimized acetylcholine sensor for monitoring in vivo cholinergic activity. *Nat. Methods* **17**, 1139–1146 (2020).
8. D. Budai, "Carbon fiber-based microelectrodes and microbiosensors" in *Intelligent and Biosensors*, V. Somerset, Ed. (InTech, 2010), pp. 269–288.
9. M. Koenig, A. Thinnes, J. Klein, Microdialysis and its use in behavioural studies: Focus on acetylcholine. *J. Neurosci. Methods* **300**, 206–215 (2018).
10. J. Zhang *et al.*, In vivo monitoring of serotonin in the striatum of freely moving rats with one minute temporal resolution by online microdialysis-capillary high-performance liquid chromatography at elevated temperature and pressure. *Anal. Chem.* **85**, 9889–9897 (2013).
11. H. Yang, A. B. Thompson, B. J. McIntosh, S. C. Altieri, A. M. Andrews, Physiologically relevant changes in serotonin resolved by fast microdialysis. *ACS Chem. Neurosci.* **4**, 790–798 (2013).
12. H. Yang, M. M. Sampson, D. Senturk, A. M. Andrews, Sex- and SERT-mediated differences in stimulated serotonin revealed by fast microdialysis. *ACS Chem. Neurosci.* **6**, 1487–1501 (2015).
13. S. C. Altieri, A. L. Garcia-Garcia, E. D. Leonardo, A. M. Andrews, Rethinking 5-HT1A receptors: Emerging modes of inhibitory feedback of relevance to emotion-related behavior. *ACS Chem. Neurosci.* **4**, 72–83 (2013).
14. P. Song, N. D. Hershey, O. S. Mabrouk, T. R. Slaney, R. T. Kennedy, Mass spectrometry "sensor" for in vivo acetylcholine monitoring. *Anal. Chem.* **84**, 4659–4664 (2012).
15. T. Nur, S. H. Gautam, J. A. Stenken, W. L. Shew, Probing spatial inhomogeneity of cholinergic changes in cortical state in rat. *Sci. Rep.* **9**, 9387 (2019).
16. B. Si, E. Song, Recent advances in the detection of neurotransmitters. *Chemosensors (Basel)* **6**, 1 (2018).
17. M. Shen *et al.*, Single synaptic observation of cholinergic neurotransmission on living neurons: Concentration and dynamics. *J. Am. Chem. Soc.* **140**, 7764–7768 (2018).
18. F. Sun *et al.*, A genetically encoded fluorescent sensor enables rapid and specific detection of dopamine in flies, fish, and mice. *Cell* **174**, 481–496.e19 (2018).
19. P. M. Borden *et al.*, A fast genetically encoded fluorescent sensor for faithful in vivo acetylcholine detection in mice, fish, worms and flies. *bioRxiv*, https://doi.org/10.1101/2020.02.07.939504 (2020).
20. A. Muller, V. Joseph, P. A. Slesinger, D. Kleinfeld, Cell-based reporters reveal in vivo dynamics of dopamine and norepinephrine release in murine cortex. *Nat. Methods* **11**, 1245–1252 (2014).
21. Y. Xie *et al.*, Resolution of high-frequency mesoscale intracortical maps using the genetically encoded glutamate sensor iGluSnFR. *J. Neurosci.* **36**, 1261–1272 (2016).
22. J. Feng *et al.*, A genetically encoded fluorescent sensor for rapid and specific in vivo detection of norepinephrine. *Neuron* **102**, 745–761.e748 (2019).
23. T. Patriarchi *et al.*, Ultrafast neuronal imaging of dopamine dynamics with designed genetically encoded sensors. *Science* **360**, eaat4422 (2018).
24. R. Walsh, J. M. Morales, C. G. Skipwith, T. T. Ruckh, H. A. Clark, Enzyme-linked DNA dendrimer nanosensors for acetylcholine. *Sci. Rep.* **5**, 14832 (2015).
25. D. Selnihhin, S. M. Sparvath, S. Preus, V. Birkedal, E. S. Andersen, Multifluorophore DNA origami beacon as a biosensing platform. *ACS Nano* **12**, 5699–5708 (2018).
26. S. M. Douglas, I. Bachelet, G. M. Church, A logic-gated nanorobot for targeted transport of molecular payloads. *Science* **335**, 831–834 (2012).
27. H. Ijäs, I. Hakaste, B. Shen, M. A. Kostiainen, V. Linko, Reconfigurable DNA origami nanocapsule for ph-controlled encapsulation and display of cargo. *ACS Nano* **13**, 5959–5967 (2019).
28. D. Purves, J. W. Lichtman, Synaptic sites on reinnervated nerve cells visualized at two different times in living mice. *J. Neurosci.* **7**, 1492–1497 (1987).
29. R. Nirogi, K. Mudigonda, V. Kandikere, R. Ponnamaneni, Quantification of acetylcholine, an essential neurotransmitter, in brain microdialysis samples by liquid chromatography mass spectrometry. *Biomed. Chromatogr.* **24**, 39–48 (2010).
30. A. Scimemi, M. Beato, Determining the neurotransmitter concentration profile at active synapses. *Mol. Neurobiol.* **40**, 289–306 (2009).
31. F. Helmchen, W. Denk, Deep tissue two-photon microscopy. *Nat. Methods* **2**, 932–940 (2005).
32. Y. Wang *et al.*, Accurate quantification of astrocyte and neurotransmitter fluorescence dynamics for single-cell and population-level physiology. *Nat. Neurosci.* **22**, 1936–1944 (2019).
33. M. B. Robers *et al.*, A luminescent assay for real-time measurements of receptor endocytosis in living cells. *Anal. Biochem.* **489**, 1–8 (2015).
34. D. M. Quinn, Acetylcholinesterase: Enzyme structure, reaction dynamics, and virtual transition states. *Chem. Rev.* **87**, 955–979 (1987).
35. J. W. Lichtman, L. Magrassi, D. Purves, Visualization of neuromuscular junctions over periods of several months in living mice. *J. Neurosci.* **7**, 1215–1222 (1987).
36. P. A. Wiggins *et al.*, High flexibility of DNA on short length scales probed by atomic force microscopy. *Nat. Nanotechnol.* **1**, 137–141 (2006).
37. P. J. Hagerman, Flexibility of DNA. *Annu. Rev. Biophys. Biophys. Chem.* **17**, 265–286 (1988).

38. W. D. Snider, The dendritic complexity and innervation of submandibular neurons in five species of mammals. *J. Neurosci.* **7**, 1760–1768 (1987).
39. P. Ascher, W. A. Large, H. P. Rang, Studies on the mechanism of action of acetylcholine antagonists on rat parasympathetic ganglion cells. *J. Physiol.* **295**, 139–170 (1979).
40. C. M. McCann, J. W. Lichtman, In vivo imaging of presynaptic terminals and postsynaptic sites in the mouse submandibular ganglion. *Dev. Neurobiol.* **68**, 760–770 (2008).
41. E. Palma *et al*., Physiological characterization of human muscle acetylcholine receptors from ALS patients. *Proc. Natl. Acad. Sci. U.S.A.* **108**, 20184–20188 (2011).
42. S. W. Kuffler, D. Yoshikami, The number of transmitter molecules in a quantum: An estimate from iontophoretic application of acetylcholine at the neuromuscular synapse. *J. Physiol.* **251**, 465–482 (1975).
43. C. P. Montgomery, B. S. Murray, E. J. New, R. Pal, D. Parker, Cell-penetrating metal complex optical probes: Targeted and responsive systems based on lanthanide luminescence. *Acc. Chem. Res.* **42**, 925–937 (2009).
44. M. Tantama, Y. P. Hung, G. Yellen, Imaging intracellular pH in live cells with a genetically encoded red fluorescent protein sensor. *J. Am. Chem. Soc.* **133**, 10034–10037 (2011).
45. I. L. Medintz *et al*., Quantum-dot/dopamine bioconjugates function as redox coupled assemblies for in vitro and intracellular pH sensing. *Nat. Mater.* **9**, 676–684 (2010).
46. A. E. Granstedt, M. L. Szpara, B. Kuhn, S. S. H. Wang, L. W. Enquist, Fluorescence-based monitoring of in vivo neural activity using a circuit-tracing pseudorabies virus. *PLoS One* **4**, e6923 (2009).
47. R. J. Salin-Pascual, A. Jimenez-Anguiano, Vesamicol, an acetylcholine uptake blocker in presynaptic vesicles, suppresses rapid eye movement (REM) sleep in the rat. *Psychopharmacology (Berl.)* **121**, 485–487 (1995).
48. T. Suzuki, Synaptic transmission and Modulation in submandibular ganglia: Aspects of a current-clamp study. *Bull. Tokyo Dent. Coll.* **41**, 149–167 (2000).
49. H. Yawo, Rectification of synaptic and acetylcholine currents in the mouse submandibular ganglion cells. *J. Physiol.* **417**, 307–322 (1989).
50. A. B. Smith, L. Motin, N. A. Lavidis, D. J. Adams, Calcium channels controlling acetylcholine release from preganglionic nerve terminals in rat autonomic ganglia. *Neuroscience* **95**, 1121–1127 (2000).
51. C. M. McCann, J. C. Tapia, H. Kim, J. S. Coggan, J. W. Lichtman, Rapid and modifiable neurotransmitter receptor dynamics at a neuronal synapse in vivo. *Nat. Neurosci.* **11**, 807–815 (2008).
52. J. M. Morales, C. G. Skipwith, H. A. Clark, Quadruplex integrated DNA (QuID) nanosensors for monitoring dopamine. *Sensors (Basel)* **15**, 19912–19924 (2015).
53. M. Jing, Y. Zhang, H. Wang, Y. Li, G-protein-coupled receptor-based sensors for imaging neurochemicals with high sensitivity and specificity. *J. Neurochem.* **151**, 279–288 (2019).
54. C. Vinegoni, A. D. Aguirre, S. Lee, R. Weissleder, Imaging the beating heart in the mouse using intravital microscopy techniques. *Nat. Protoc.* **10**, 1802–1819 (2015).
55. R. Lorenz *et al*., ViennaRNA package 2.0. *Algorithms Mol. Biol.* **6**, 26 (2011).
56. P. Stothard, The sequence manipulation suite: JavaScript programs for analyzing and formatting protein and DNA sequences. *Biotechniques* **28**, 1102–1104, 1104 (2000).
57. G. L. Ellman, K. D. Courtney, V. Andres Jr, R. M. Feather-Stone, A new and rapid colorimetric determination of acetylcholinesterase activity. *Biochem. Pharmacol.* **7**, 88–95 (1961).
58. P. R. Heenan, T. T. Perkins, Imaging DNA equilibrated onto mica in liquid using biochemically relevant deposition conditions. *ACS Nano* **13**, 4220–4229 (2019).
59. X. Qi *et al*., Programming molecular topologies from single-stranded nucleic acids. *Nat. Commun.* **9**, 4579 (2018).